Hydroxyapatite Microparticles as Feedback-Active Reservoirs of Corrosion Inhibitors

D. Snihirova,[†] S. V. Lamaka,[*,†] M. Taryba,[†] A. N. Salak,[‡] S. Kallip,[‡] M. L. Zheludkevich,[‡] M. G. S. Ferreira,[†,‡] and M. F. Montemor[†]

ICEMS, Instituto Superior Tecnico, UTL, Avenida Rovisco Pais, 1049-001 Lisbon, Portugal, and CICECO, Dep. of Ceramics and Glass Engineering, University of Aveiro, 3810-193 Aveiro, Portugal

ABSTRACT This work contributes to the development of new feedback-active anticorrosion systems. Inhibitor-doped hydroxyapatite microparticles (HAP) are used as reservoirs, storing corrosion inhibitor to be released on demand. Release of the entrapped inhibitor is triggered by redox reactions associated with the corrosion process. HAP were used as reservoirs for several inhibiting species: cerium(III), lanthanum(III), salicylaldoxime, and 8-hydroxyquinoline. These species are effective corrosion inhibitors for a 2024 aluminum alloy (AA2024), used here as a model metallic substrate. Dissolution of the microparticles and release of the inhibitor are triggered by local acidification resulting from the anodic half-reaction during corrosion of AA2024. Calculated values and experimentally measured local acidification over the aluminum anode (down to pH = 3.65) are presented. The anticorrosion properties of inhibitor-doped HAP were assessed using electrochemical impedance spectroscopy. The microparticles impregnated with the corrosion inhibitors were introduced into a hybrid silica−zirconia sol−gel film, acting as a thin protective coating for AA2024, an alloy used for aeronautical applications. The protective properties of the sol−gel films were improved by the addition of HAP, proving their applicability as submicrometer-sized reservoirs of corrosion inhibitors for active anticorrosion coatings.

KEYWORDS: hydroxyapatite • corrosion inhibitor • sol−gel coating • AA2024 • pH microscopy

INTRODUCTION

Corrosion is a major issue for various industries where metals are used as structural and functional materials. It is one of the major reasons for energy and material loss during the service life of many engineering structures. Global annual cost of corrosion is estimated to be around 4.2% of the gross national products (approximately $100 billion in USA and around €200 billion in Europe) (1, 2). One of the most widespread strategies for corrosion protection of metallic parts is the application of protective polymeric coatings, which generally consist of several layers, of which the most important are pretreatment, primer, and topcoat.

Recently, hybrid organic−inorganic sol−gel films have been suggested as effective intermediate protective layers (e.g., by combining the pretreatment and primer into one single layer), ensuring a good adhesion between the organic topcoat and the metallic substrate. Moreover, a sol−gel layer also provides an additional dense barrier that restricts the ingress of corrosive species (1, 3). However, sol−gel films cannot impart any active corrosion protection (4), failing to stop propagation of corrosion processes when defects occur in the coating system. The introduction of anticorrosion components into sol−gel films can be one of the ways to develop coatings with active corrosion protection ability. A number of different approaches have been proposed to introduce an inhibitor in the pretreatment or primer layers. Direct doping of the thin sol−gel layer with inhibiting ions or molecules can impart effective corrosion protection, provided that the inhibitor does not interact with the components of the sol−gel formulation (5). Otherwise, the barrier properties of the sol−gel film can be disrupted, and the inhibiting ability of the chemically modified inhibitor decreased or was even lost (6, 7). One more drawback of this approach is early leakage of the inhibitor and consequent loss of its effectiveness (8).

Storing inhibitors inside nano- and microreservoirs uniformly distributed in the coating can overcome the above-mentioned limitations of direct doping. Such an approach prevents contact of the inhibitor with the coating matrix, avoiding detrimental inhibitor−coating interactions (6). Recent advances in nanotechnology paved the way for establishing a variety of micro- or nanostructures that can serve as host reservoirs for corrosion-inhibiting guest species. The development and application of inhibitor-doped containers for self-healing protective coatings was reviewed by Shchukin et al. (9, 10). Among the possible reservoirs, the most suitable are porous (11, 12) or hollow (13) particles and their assemblies (14). They can be constructed in such a way as to release the inhibitor when electrolyte reaches the metal surface and the corrosion process commences. In this case, the mechanism of active protection can be described as follows: (i) cathodic and anodic half-reactions of the corrosion process change the local pH (alkalinization over the

* Corresponding author. E-mail: sviatlana.lamaka@ist.utl.pt.
Received for review February 17, 2010 and accepted September 27, 2010
[†] Instituto Superior Tecnico, UTL.
[‡] University of Aveiro.
DOI: 10.1021/am1005942
2010 American Chemical Society

cathode and slight acidification over the anode); (ii) these changes provide the stimulus to release the inhibitor from the reservoirs; (iii) the inhibitor diffuses to the active area and forms a sufficiently inhibiting and stable film; (iv) the inhibiting layer decreases the corrosion activity and the pH returns to neutral; (v) the stimulus subsides and the reservoirs become inhibitor storage again, ready to release inhibitor as soon as another corrosion event occurs.

The pH sensitivity of the reservoirs can be achieved, for example, by using weak polyelectrolytes assembled in a layer-by-layer approach (15). The layers of oppositely charged polyelectrolytes deposited on nanoparticles, or directly into the sol−gel coating, form a shell, preventing undesired leakage of the inhibitor. Controlled release of the inhibiting species from the host structure occurs when conformation of the polyelectrolyte molecules changes because of changes in the local pH (6, 16). Another release mechanism related to the pH sensitivity is the partial or complete dissolution of the reservoirs when a specific pH is reached at the anodic or cathodic sites.

To be efficient, the inhibitor reservoirs must fulfill a number of requirements, among which the most important are (i) chemical and mechanical stability, (ii) compatibility with the coating matrix, (iii) sufficient loading capacity, (iv) effective storage of the inhibitor, (v) ability to sense corrosion onset, and (vi) release of the inhibitor on demand. Hydroxyapatite microparticles (HAP) fulfill these requirements: they are crystalline, water-insoluble, and submicrometer-sized, are prone to dissolution as the pH shifts to the acidic range, and possess a high surface area and, consequently, a high loading capacity. Recently, HAP were reported to be used for the corrosion protection of pure magnesium and AZ series alloys. HAP directly synthesized on a magnesium substrate in an aqueous solution demonstrated a remarkable anticorrosion performance (17). Moreover, the inhibiting action of the phosphate ions of HAP was found to prevent the corrosion of steel (18). The HAP used in this work were previously characterized and reported as drug-delivery systems for biomedical purposes (19, 20).

The aim of this work was to explore the potential of HAP to serve as pH-sensitive reservoirs to store corrosion inhibitors. Cerium (Ce^{3+}) and lanthanum (La^{3+}) cations, salicylaldoxime (Sal), and 8-hydroxyquinoline (8HQ), known to be efficient inhibitors in the corrosion protection of aluminum (21, 22), were loaded into the HAP. Inhibitor-doped microparticles were added to a sol−gel formulation, which was, in turn, applied to AA2024 coupons. This work covers the detailed assessment of the required properties of the HAP, including morphology, inhibitor storage capacity, pH sensitivity for release, and anticorrosion efficiency of the inhibitor-doped HAP.

EXPERIMENTAL SECTION

2.1. Synthesis of HAP. Calcium-deficient HAP were synthesized by mixing aqueous solutions of calcium nitrate and ammonium hydrophosphate. Citric acid was added to modify the morphology of the microparticles. Precipitation was carried out by slowly increasing the calcium and phosphate concentrations as follows: 500 mL of solution was prepared by dissolving 0.5 mol of citric acid in deionized water ($\rho > 18$ MΩ cm). The pH of the solution was adjusted to 8.5 using an ammonium hydroxide solution (25%). Then, 0.04 mol of $Ca(NO_3)_2 \cdot 4H_2O$ was gradually added to the citric acid solution. A total of 200 mL of a 0.2 M $(NH_4)_2HPO_4$ solution was prepared in deionized water and mixed with the one described above. The obtained calcium phosphate−citrate supersaturated solution was placed in a water bath and kept at 37 °C for 24 h, allowing HAP precipitation. The microparticles were separated from the solution by filtration through a 0.22-μm Millipore filter and dried in a desiccator.

To load the corrosion inhibitors, HAP were immersed in an aqueous solution containing 1 g/L of the inhibiting compound and ultrasonically stirred. Four solutions were prepared: cerium(III) nitrate, lanthanum(III) nitrate, salicylaldoxime (Sal), and 8-hydroxyquinoline (8HQ; puriss or better grade products of Sigma Aldrich). After 24 h of soaking, the suspensions were filtered using a 0.22-μm Millipore filter and washed with deionized water. Then, the inhibitor-doped particles were placed in a desiccator for 6−7 h.

2.2. Preparation of AA2024 Substrates. The 2024-T3 aluminum alloy, the composition of which is described elsewhere (22), was used as a substrate to assess the anticorrosion protection performance of the HAP doped with corrosion inhibitors. The coupons of AA2024 were chemically etched, using a three-step cleaning procedure as generally applied in the aeronautical industry. The specific treatment was done as follows: alkaline cleaning in Metaclean T2001 at 60−70 °C for 15−25 min, followed by alkaline etching in TURCO Liquid Aluminetch N2 at 60 ± 5 °C for 30−60 s and acid etching in TURCO Liquid Smutgo NC at 30 ± 5 °C for 5−10 min. The coupons were briefly immersed (<1 min) in deionized water after each step to remove the reaction products.

2.3. Synthesis of the Sol−Gel Coatings Doped with HAP. The organic−inorganic films were synthesized using a controllable sol−gel route by mixing two different sols. An organosiloxane alkosol was combined with another alkosol containing a zirconia precursor in order to obtain the final hybrid sol. The silane-based alkosol was prepared through hydrolysis of (3-glycidoxypropyl)trimethoxysilane in 2-propanol adding a diluted aqueous solution of HNO_3 (pH = 0.5) in an 8:8:1 volume ratio, under stirring, at room temperature, during 1 h. The second alkosol, containing the zirconia nanoparticles, was prepared through controlled stoichiometric acidic hydrolysis (pH = 0.5) of a 70 wt % 2-propanol solution of zirconium(IV) tetrapropoxide in complexing agent ethyl acetoacetate (1:1 volume ratio) under ultrasonic agitation. Finally, the two alkosols were mixed in a 2:1 volume ratio, respectively. The hybrid solution was ultrasonically agitated for 1 h and then aged for another 1 h at room temperature.

Part of the solution was kept unaltered to produce reference blank samples. Another part was used to prepare the coatings loaded with HAP. A sample of 0.2 wt % (relative to the weight of the sol−gel) of HAP was added to the sol−gel solution under ultrasonic stirring for 20 min. Finally, four sol−gel coatings were prepared: a blank coating (without additives), a coating loaded with blank particles (no inhibitor), and two coatings loaded with particles filled with two different corrosion inhibitors: Ce^{3+} and Sal.

To ascertain the influence of the HAP and the inhibitors on the barrier and active properties of the coatings, two sol−gel formulations doped with two different inhibitors were also synthesized. Either Sal or $Ce(NO_3)_3$ was added to the hybrid solution after aging and ultrasonically stirred for 20 min. The sol−gel films were applied on AA2024 coupons by dip-coating, using a withdrawal rate of 18 cm/min and an emersion time in the solution of 100 s. Then, all of the coupons were cured at 120 °C for 80 min in air for cross-linking and solvent evaporation.

2.4. Techniques. 2.4.1. ***Microscopic Characterization. Scanning Electron Microscopy/Energy-Dispersive X-ray Spectroscopy (SEM/EDS).*** The microstructure, qualitative chemical composition, and thickness of the sol−gel coatings were studied by SEM coupled with EDS. A semi-in-lens Hitachi SU-70 UHR Schottky (Analytical) field-emission SEM microscope coupled with a Bruker EDS detector was used. An FE-SEM JEOL 7001 apparatus was also used for SEM observation.

Atomic Force Microscopy (AFM). The morphology and behavior of HAP in varying conditions of acidity were studied in situ by AFM, using an Agilent Technologies 5100 system. AppNano silicon probes were used. The HAP were dispersed in 0.05 M NaCl by a brief ultrasonic application before their introduction into the AFM liquid cell. A freshly cleaved mica (001) plane was used as a flat substrate in order to visualize precipitated HAP. During the experiments, calculated amounts of HCl were injected into the AFM test cell using a micropipette to adjust the pH to specific values. Nanotec Electronica WSxM (23) software was used for image processing.

2.4.2. ***Analytical Techniques. High-Performance Liquid Chromatography (HPLC).*** HPLC was used to determine the loading capacity of HAP for 8HQ and Sal and measure release at different pHs. A PerkinElmer 200LC pump, a UV detector, and a Grace Smart RP-18 (4.6 × 250 mm, 5 μm) column were used. For experimental details, see the Supporting Information (SI).

Inductively Coupled Plasma Atomic Emission Spectroscopy (ICP-AES). ICP-AEP (Perkin Elmer Optima 2000 DV) was used to quantify the loading capacity of HAP for $Ce^{3+}$and La^{3+} and the Ca/P ratio of synthesized HAP and to study the release of preloaded inorganic inhibitors as a function of the pH.

The ζ-potential and size distribution measurements were performed using a Zetasizer Nano ZS (Malvern Instruments) system. Dynamic light scattering mode was used for particle size analysis and the laser Doppler electrophoresis mode for ζ potential. Either HCl or NaOH solution was added to the HAP suspension to change the pH.

2.4.3. ***Electrochemical Techniques. EIS.*** The electrochemical impedance spectroscopy (EIS) measurements were performed using a Gamry FAS2 femtostat with a PCI4 controller in a frequency range from 1×10^4 to 2.6×10^{-3} Hz. All of the spectra were recorded at open-circuit potential while a 10 mV sinusoidal perturbation was applied. A conventional three-electrode cell was used, consisting of a saturated calomel reference electrode, a platinum coiled wire as the counter electrode, and the AA2024 substrate as the working electrode. The area of the working electrode was approximately 3.3 cm^2. The cell was placed in a faraday cage to avoid interference with external electromagnetic fields and stray currents. EIS measurements were carried out on uncoated AA2024 coupons immersed in an aqueous solution of 0.05 M NaCl doped with HAP. The protection ability of the sol−gel-coated coupons was assessed during immersion in 3% NaCl. The electrolyte in the cell (total volume 10 mL) was quiescent and equilibrated with air. All of the measurements were performed at room temperature.

Scanning Ion-Selective Electrode Technique (SIET). An Applicable Electronics (USA) commercial SIET system controlled by the ASET program (Sciencewares) was used. For the preparation of pH-selective microelectrodes, see SI. The microelectrodes demonstrated a stable and reproducible potential in the pH range 2−10 with a linear response slope of −54.8 ± 0.7 mV/pH. The local activities of H^+ were mapped 20 μm above the surface on a 31 × 31 grid in a 0.05 M NaCl solution under open-circuit potential conditions. The time of acquisition for each data point was 2.5 s, resulting in a total scan time of about 1 h. The sample was composed of oblong pieces of pure copper and aluminum (Goodfellow; Cu foil, 99.999%; Al wire, 99.5%) electrically connected and embedded in an epoxy mold and polished after solidification.

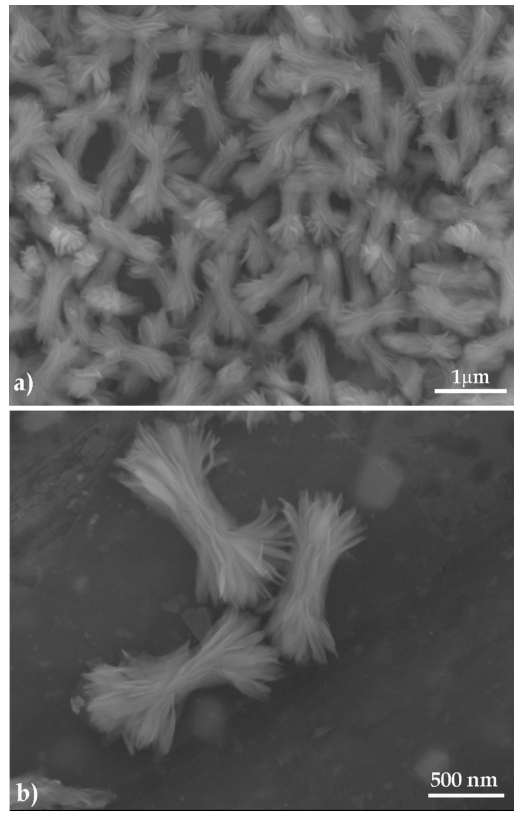

FIGURE 1. SEM micrographs of the blank HAP.

RESULTS AND DISCUSSION

3.1. Characterization of HAP. The blank HAP are presented in Figure 1. The bowtie-shaped submicrometer-sized particles are composed of smaller needlelike structures bundled together (Figure 1b). The particle size distribution is shown in Figure 2a. The HAP consist of two fractions with a respective mean size of approximately 200 and 850 nm. According to the results of ζ-potential measurements, HAP possess a negative surface charge, which drops as the pH is increased (Figure 2b). This can be explained by the adsorption of Cit^{3-} anions on the precipitated particles. Precipitation was carried out from the bittern containing 0.71 M citric acid at pH = 8.5. Such a pH favors the dominance of Cit^{3-} anions in the $H_3Cit-H_2Cit^--HCit^{2-}-Cit^{3-}$ equilibrium (24). Adsorbed Cit^{3-} anions may cause an overall negative surface charge of the microparticles. The presence of absorbed Cit^{3-} in the HAP was confirmed by Fourier transform infrared (FTIR; Figure S1 in the SI).

Different mechanisms for inhibitor retention can be expected for inorganic (Ce^{3+} and La^{3+}) (21) and organic (Sal and 8HQ) inhibitors (18). Most probably Ce^{3+} and La^{3+} cations entered HAP via an ion-exchange mechanism, changing the particles' morphology (Figure 3a,b) and crystalline structure (see Figure S2 in the SI). According to the results of SEM/EDS measurements, approximately 73 atom % of Ca^{2+} in the HAP is substituted by Ce^{3+} and 60 atom % of Ca^{2+} is substituted by La^{3+}. The results of ICP-AES measurements revealed that the loading capacities of the HAP were approximately 22 and 20 wt % for Ce^{3+} and La^{3+}, respectively.

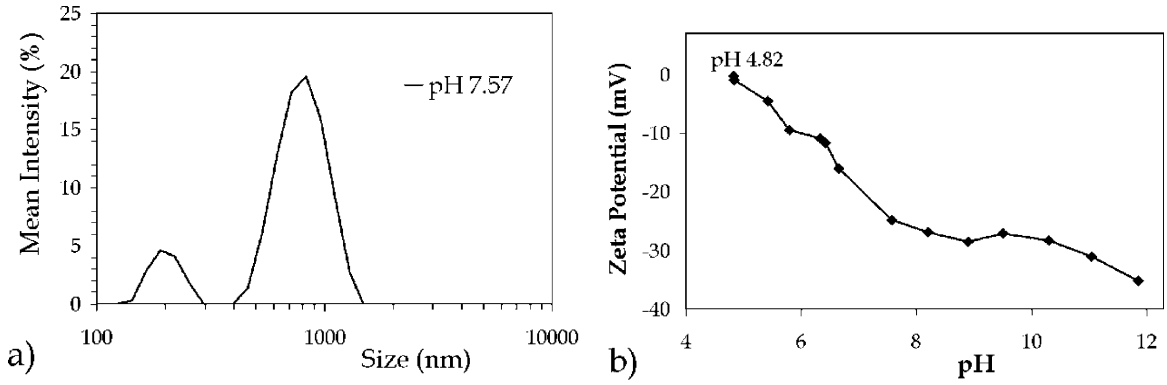

FIGURE 2. (a) HAP size distribution at pH = 7.57. (b) pH dependence of the ζ potential of HAP.

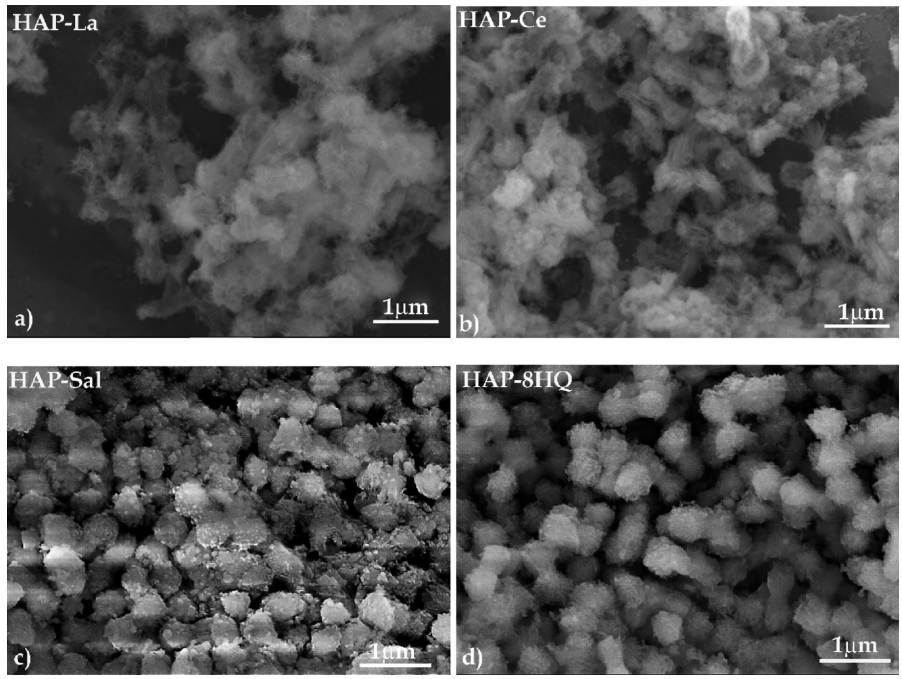

FIGURE 3. SEM images of HAP loaded with (a) Ce^{3+}, (b) La^{3+}, (c) Sal, and (d) 8HQ.

The organic inhibitors, Sal and 8HQ, are likely to be adsorbed, inducing only slight changes in the HAP morphology as shown in Figure 3c,d. Moreover, only slight changes were detected in the crystalline structure of the HAP (Figure S2 in the SI). The loading capacity for Sal is 0.54 wt %, and that for 8HQ is 9.3 wt %, as determined by HPLC. Such a difference in loading capacities for Sal and 8HQ can probably be explained by the different affinities of the inhibitors for Ca. 8HQ forms stable complexes with Ca: $\log K^{1}_{Ca(8HQ)_2} = 3.27$ (24). Meanwhile, no data about the formation of Ca complexes with Sal could be found (25). To the contrary, some reports suggest that Ca does not interfere in the determination of Al^{3+}, Zn^{2+}, Fe^{3+}, etc., with Sal (26).

XRD analysis was performed in order to assess the changes in the crystalline structure of the hydroxyapatite after doping with different inhibiting compounds. Blank HAP and the hydroxyapatite powders treated with Sal and lanthanum nitrate (HAP-Sal and HAP-La^{III}) were characterized. The diffraction patterns of HAP and HAP-Sal show that treatment with Sal does not change the crystalline structure of hydroxyapatite (see Figure S2 in the SI). Treatment with lanthanum results in decomposition of the hydroxyapatite phase. HAP-La^{III} presents a mixture of calcium- and lanthanum-based phases, where calcium phosphate oxide [$Ca_{10}(PO_4)_6O$] and lanthanum phosphate ($LaPO_4$) are the dominant compounds. The XRD data were refined using the monoclinic symmetry (space group $P2_1/b$); crystal structure parameters are presented in Table S1 in the SI.

It is known that variation in the Ca/P atomic ratio (e.g., in nonstoichiometric hydroxyapatites) leads to a change in the lattice parameters (27). The Ca/P ratio of the HAP was 1.57, as determined by analytical SEM/EDS, and 1.62, according to the results of ICP-AES. Thus, the difference between the values observed in this work and those previously reported is likely to result from deviations from the nominal composition of $[Ca_5(PO_4)_3(OH)]_2$ due to the peculiarity of the HAP synthesis described above.

The pH dependence of the inhibitor release from the HAP is shown in Figure 4. HAP preloaded with inorganic inhibitors start to release the inhibitors at a pH below 6, with an acceleration of Ce^{3+} and La^{3+} release when the pH falls below 3.1. The release trend for Sal and 8HQ is different: it

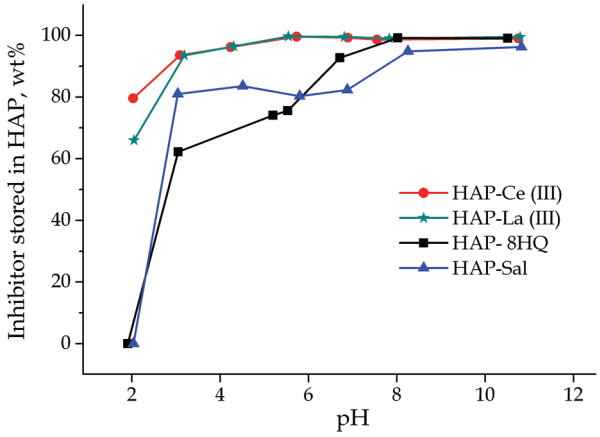

FIGURE 4. Release of different inhibitors from the HAP as a function of the pH. The curves show the amount of inhibitor remaining in the HAP after 24 h of immersion in a 0.05 M NaCl solution at specified pHs.

begins at a slightly alkaline pH and ends with 100% release at pH = 2 along with the complete dissolution of the HAP. The results suggest that the organic inhibitors did not change the crystalline structure of submicrometer-sized HAP, while the inorganic cations have a marked effect over it. The difference can be explained by the adsorption (organic) or ion-exchange (inorganic) mechanisms of loading inhibitors into the HAP.

3.2. Corrosion Inhibition Properties of HAP on Bare AA2024. The role of the HAP as reservoirs of anticorrosion species is to deliver inhibitor on demand and to ensure active corrosion protection when corrosion breaks through. The anticorrosion ability of HAP was studied by immersing bare coupons of AA2024 in 0.05 M NaCl corrosive electrolyte, containing 2 g/L of the blank and inhibitor-doped HAP. The frequency dependence of the complex impedance of a bare aluminum alloy immersed in an electrolyte allows for evaluation of the different components of the electrochemical system such as the state of the native oxide, polarization resistance, and double-layer capacitance, which are related to electrochemical corrosion activity.

Figure 5 shows the results of the electrochemical impedance measurements after 1 h of immersion. The impedance spectra are characterized by a resistive response in the high-frequency range that can be assigned to the electrolyte resistance. Then a capacitive slope is observed, extending over a wide frequency range. At very low frequencies, a new resistive plateau takes shape. This low-frequency part of the impedance spectra can be correlated with the extent of corrosion activity. Higher impedance values reveal higher corrosion protection, whereas lower values account for stronger corrosion activity. As shown in Figure 5a, the lowest values of the low-frequency impedance were detected for AA2024 coupons immersed in a 0.05 M NaCl solution without particles. The phase-angle plots obtained in the solutions containing the HAP are characterized by a broad time constant (Figure 5b). The phase angle reaches −90° and in the low-frequency range starts increasing because of the resistive response. However, the coupon exposed to the blank solution presents a new time constant in the low-

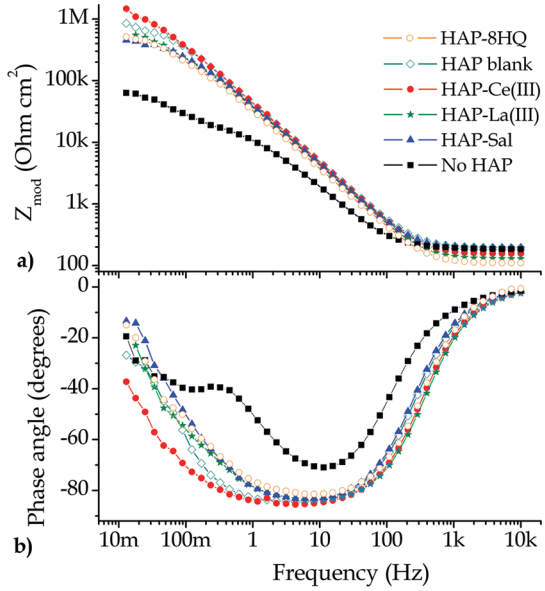

FIGURE 5. Electrochemical impedance Bode plots taken after 1 h of immersion of AA2024 specimens in a suspension of inhibitor-doped HAP in 0.05 M NaCl.

frequency range (around 0.1 Hz), indicating the onset of the corrosion processes. Notably, all samples tested in the presence of blank and inhibitor-doped HAP reveal a marked inhibiting effect. Ce^{3+}-doped and blank HAP showed the highest low-frequency impedance values and, therefore, the highest inhibiting efficiency. Sal-, 8HQ-, and La^{3+}-doped particles also inhibit the corrosion process, showing low-frequency impedance values almost 1 order of magnitude higher than those measured for the alloy immersed in the electrolyte without HAP.

3.3. Protective Performance of Sol−Gel Coatings Modified with HAP. HAP doped with corrosion inhibitors were introduced in the sol−gel coating to verify their compatibility with the coating matrix and assess the effect of active anticorrosion protection. The average thickness of the sol−gel coating deposited on the AA2024 coupons was around 1.8−2.0 μm. The SEM images depicted in Figure 6a and the EDS distribution of calcium and phosphorus depicted in Figure 6b show that HAP added to the sol−gel precursor solution are homogeneously distributed in the sol−gel matrix after application on the metallic substrate and curing.

No particle agglomerates were found. The embedded particles are compatible with the coating and do not induce mechanical defects, pores, or pinholes. Figure 6c shows the three-dimensional distribution of the HAP in the same sol−gel coating. The image was obtained by exposing a 10 × 10 μm area of the coating surface to a focused ion beam (FIB) using a Zeiss Neon 40 apparatus. During the course of defect formation, silane-based hybrid coating was etched considerably faster than HAP. Thus, each microscopic pillar in Figure 6c is composed of the sol−gel "rod" with one HAP on top. A SEM image of a FIB defect clearly shows homogeneous distribution of the HAP along the full depth of the sol−gel coating.

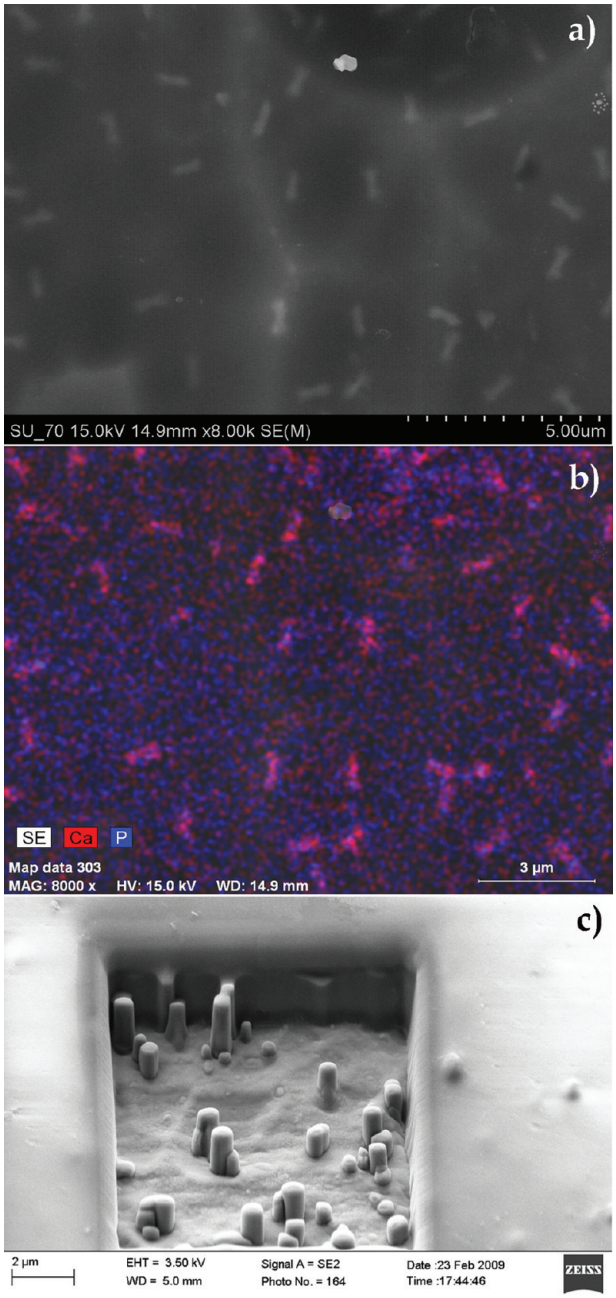

FIGURE 6. (a) SEM micrograph of the sol−gel coating doped with HAP deposited on AA2024. (b) EDS elemental distribution of Ca and P. (c) Three-dimensional spatial distribution of HAP in the sol−gel coating obtained by the FIB technique.

The corrosion resistance of samples coated with blank sol−gel, sol−gel doped with blank particles, and particles doped with corrosion inhibitors was tested by EIS during immersion in 3% NaCl. The selected Bode plots, obtained at the beginning and after 1 week of immersion, are shown in Figure 7. The Bode plots are characterized by the presence of a time constant in the high-frequency region, related to the barrier properties of the sol−gel coating. A time constant observed in the middle frequencies (1−0.1 Hz) is related to the presence of an intermediate protective oxide layer, underneath the coating. The blank coating shows the highest depression for this time constant and, therefore, disruption of the protective oxide layer.

The active component of anticorrosion protection can be analyzed through appraisal of the low-frequency region of the impedance spectra. The blank sol−gel coating presents the lowest impedance values after 1 week of immersion, and the impedance of the sol−gel loaded with inhibitor-doped HAP is higher than that of the sol−gel with the undoped HAP. The sol−gel coating without particles and the sol−gel coating modified with the blank HAP show the presence of a third time constant in the lowest-frequency region that accounts for corrosion activity. Conversely, no signs of corrosion were found in the impedance spectra for the sol−gel loaded with Sal and Ce^{3+}-doped HAP after 1 week of immersion. The sol−gel coatings containing HAP modified with corrosion inhibitors show a capacitive behavior at low frequencies, revealing that the oxide layer beneath the sol−gel coating was not disrupted by the aggressive agents (36). The overall impedance of these coatings is above 5 MΩ cm^2 after 1 week of immersion, emphasizing the protective properties of the HAP-doped coatings. As corrosion starts, the pH drops, the HAP partly dissolve, and the entrapped inhibitor is released. The inhibitor reaches the active corrosion sites, forms an inhibiting layer, and hinders further corrosion activity. The increased low-frequency impedance measured for the samples coated with sol−gel containing inhibitor-doped HAP (Figure 7) clearly confirms that the active protection effect originated from the inhibitors released from the HAP. For a quantitative estimation of the protective properties of the sol−gel films modified with HAP, experimental impedance spectra were fitted with an equivalent circuit, which simulates the response of the coated aluminum alloy (Figure 7c). Constant phase elements (CPEs) instead of pure capacitances were used for fitting of the experimental spectra. Such a modification is preferable if the phase angle shifts from −90°, the value expected for a pure capacitive behavior. In the equivalent circuit, R_{sol} is the resistance of the electrolyte, the 0.3% NaCl solution. The R_{SG}/CPE_{SG} accounts for the barrier properties of the sol−gel coating and R_{OX}/CPE_{OX} for the protective properties of the intermediate oxide layer, and finally R_{polar}/CPE_{DL} values are assigned to the charge-transfer resistance and double-layer capacitance in the active defects that formed in the oxide and activate the metallic substrate. Figure 8 presents the evolution of the different parameters, extracted from a numerical fitting of the experimental spectra. Figure 8a reveals a fast drop of the sol−gel coating resistance, R_{SG}, during the early immersion stages in the NaCl solution. Such a trend was expected and is usually observed for this type of sol−gel coating (11−13). Electrolyte uptake through the nanosized pores of the coating is responsible for the sol−gel's resistance drop.

Interpretation of the impedance spectra (Figure 7a,b) and their accurate fitting revealed that the HAP-free sol−gel coating reveals a slightly higher resistance. Given that the coating thickness was equal for all samples and that the SEM observations did not reveal any defects in the coating induced by the incorporated HAP, lower R_{SG} of the HAP-doped coating (Figure 8a) may account for certain changes

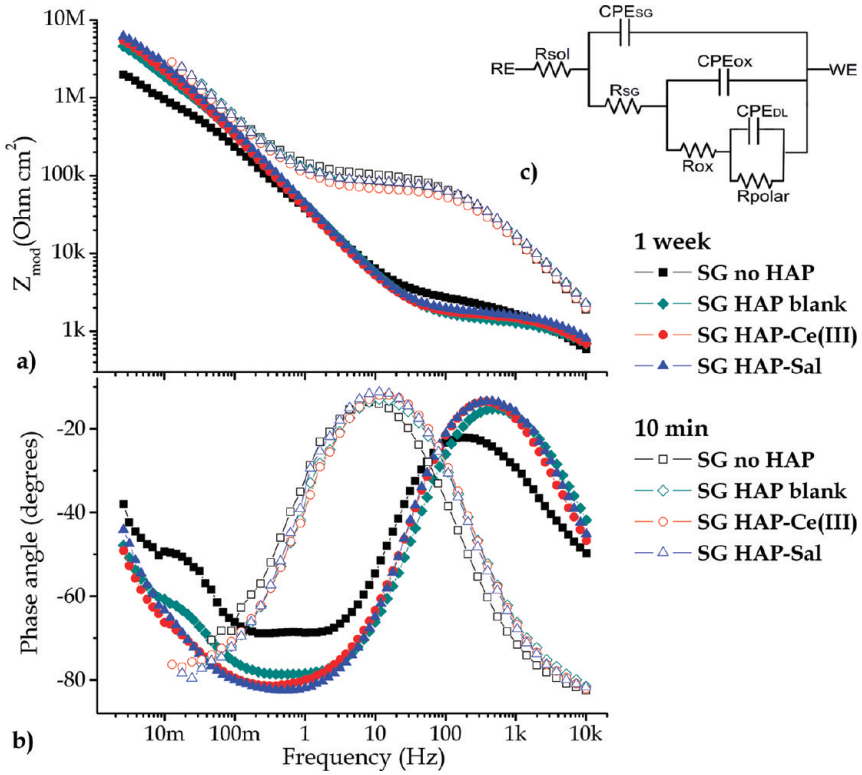

FIGURE 7. (a and b) Bode plots for the sol–gel-coated AA2024 samples after 10 min and 1 week of immersion in a 3% NaCl solution. (c) Equivalent circuit used for fitting of the experimental EIS spectra.

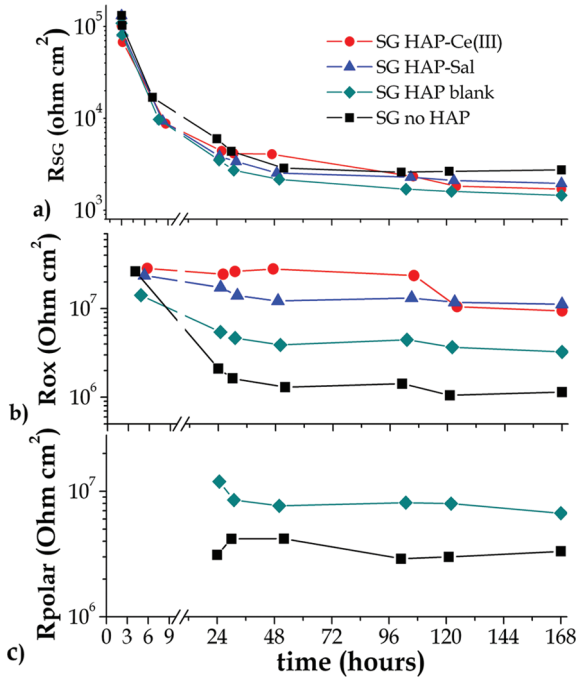

FIGURE 8. Evolution of the parameters of the corrosion process in the sol–gel-coated AA2024 samples during 1 week of immersion in a 3.0% NaCl neutral solution: (a) resistance R_{SG} of the HAP-doped sol–gel films; (b) resistance of the native oxide film R_{OX}; (c) polarization resistance R_{polar}.

in the course of the sol–gel synthesis. It is well-known that silicon alkoxides are not very reactive, and a catalyst should be added to promote hydrolysis–condensation reactions (4). The sol–gel was obtained by acid-catalyzed hydrolysis of the sol–gel precursors. However, HAP suspensions added to some sol–gel formulations have pH = 7.0–7.8, depending on the adsorbed inhibitor, thus changing the optimized conditions of sol–gel gelation.

Nonetheless, the inhibitors stored in the HAP compensate comprehensively for the slight decrease of the sol–gel barrier properties. The decrease of R_{OX} (Figure 8b) indicates the fastest deterioration of the native oxide layer for the sample without HAP. From roughly the same initial values of R_{OX}, this parameter becomes 1 order of magnitude higher for the alloy coated with the sol–gel containing inhibitor-doped HAP (compared to the blank sol–gel) by the end of immersion testing. The values of the polarization resistance, R_{polar}, could be quantified only for inhibitor-free sol–gel coatings because the corrosion process was suppressed in the samples coated with the sol–gels containing Ce- and Sal-doped HAP (Figure 8c). The lowest values were measured for the blank coating, thus revealing higher corrosion activity in the defects formed in the oxide layer.

It is interesting that, although the loading capacity for Ce^{3+} is 37 times that for Sal, both species exhibit similar inhibiting effects. A plausible explanation for this fact arises from the different release trends and different inhibiting mechanisms of the two inhibitors. As shown in Figure 4, around 20% of the preloaded Sal is released from the HAP at a pH in the range of 7.0–3.1, while the Ce^{3+} amount of released inhibitor in the same pH range is between 1 and 7%. This effect offsets the difference between the loading capacities. Moreover, it is shown in the literature (21, 22) that Ce^{3+} and La^{3+} inhibit a cathodic reaction, precipitating corresponding hydroxides in the sites with high local pH. Sal and 8HQ are more effective at hindering anodic dissolution

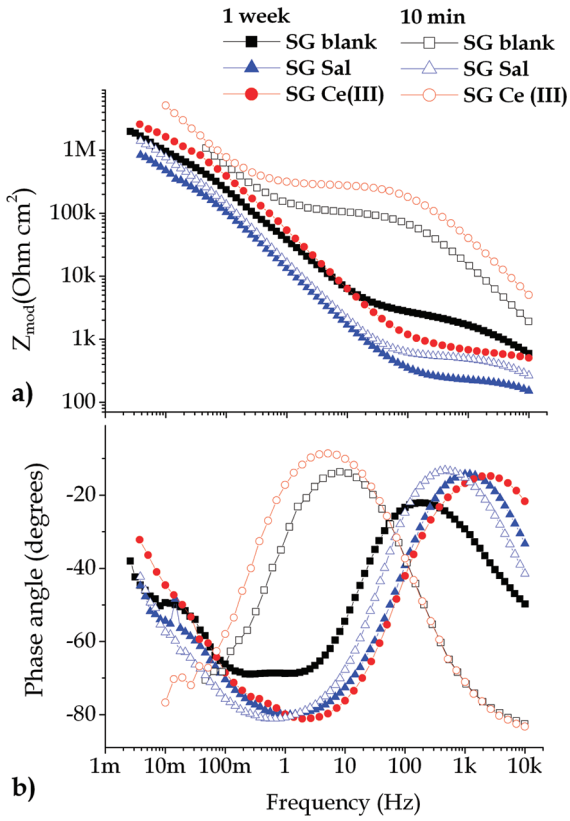

FIGURE 9. (a and b) Bode plots for the HAP-free sol−gel deposited on AA2024 samples. The inhibitors, Ce^{3+} and Sal, were directly added to the sol−gel formulation during synthesis.

because they form insoluble chelates with Al^{3+}. Given that cathodic and anodic reactions are usually separated by a microdistance and Ce^{3+} cations are released in anodically active sites, it is logical to assume that a higher amount of dissolved Ce^{3+} is necessary to reach the cathodic sites compared to Sal.

The AA2024 sample coated with the blank sol−gel shows the highest rate of degradation, while specimens covered with the sol−gel doped with inhibitor-loaded HAP demonstrate better corrosion protection. Thus, the inhibitor incorporated into the particles keeps its activity and does not disturb the integrity of the sol−gel matrix when released. The results illustrate that the inhibitor-doped HAP can be used as active, pH-sensitive reservoirs for corrosion inhibitors.

To clarify the influence of the HAP and the inhibitors on the barrier and active properties of the coatings, Figure 9 presents the Bode plots for the Ce^{3+}- and Sal-containing samples without HAP; the inhibitors were directly added to the sol−gel before deposition on AA2024. The amounts of the two added inhibitors were different, corresponding to the loading capacity of the inhibitor-doped HAP. Presented measurements were taken after 10 min and 1 week of immersion in a 3% NaCl neutral solution. Although the addition of Ce^{3+} improves the barrier properties of the sol−gel film at the beginning of the immersion test, the resistance of the sol−gel film drops below that for the blank sol−gel after 1 week of immersion. Direct doping of the sol−gel formulation with Sal leads to a significant deterioration of the barrier properties of the sol−gel film.

Thus, this experiment confirms that direct doping of the sol−gel film with the inhibitors may likely cause deterioration of the barrier properties of the coating. This effect can probably be attributed to interaction of the coating precursors with the inhibitor, which disrupts the hydrolysis and condensation reactions during the sol−gel synthesis and leads to deactivation of the inhibitor. Contrary to that, modifying a sol−gel formulation with inhibitor-doped particles does not allow for uncontrolled interaction of the sol−gel and inhibitor. In this case, neither the barrier properties of the coating are damaged nor is the inhibitor's potency diminished. It also has to be emphasized that interaction of each individual inhibitor with each coating formulation is a unique chemical process, which is not easily predicted and has to be considered individually for each particular combination of coating, inhibitor, and inhibitor concentration. For example, it was shown that Ce^{3+} and 8HQ may either improve or worsen the barrier properties of the sol−gel depending on the stage of the sol−gel synthesis when the inhibitor is added (7, 28−30). Benzotriazole always disrupts the coating integrity no matter at which stage it is added (6, 30). Vanadate ($NaVO_3$) also damages the barrier properties of the hybrid sol−gel film (7, 31). Meanwhile, the idea of a pH-triggered inhibitor release from the HAP (or other reservoirs) will be applicable for any inhibitor-coating combination.

3.4. pH-Dependent Behavior of HAP. Despite the different mechanisms for inhibitor retention suggested by XRD analysis, the results of impedance measurements presented in Figure 5 reveal similar inhibiting action of the HAP doped with Sal, 8HQ, La^{3+}, and Ce^{3+}. Moreover, the impedance measurements clearly evidence that the blank HAP cannot be considered as inert hosts. The blank HAP also inhibit the corrosion activity of AA2024. A plausible explanation for such behavior could be the pH buffering properties of the HAP. To better assess the mechanisms of active corrosion protection, AFM scans of the HAP without inhibitor were taken in situ. The pH-dependent behavior of the HAP and their pH buffering effect were studied by scanning the same microparticles at different pHs. As shown in Figure 2a, the HAP are divided into two fractions, one with a mean particle size of 200 nm and another with a mean particle size of approximately 850 nm. A zone on the mica with only a smaller size fraction, 200 nm, was chosen for AFM scanning at different pHs because its roughness was significantly lower. The smaller particles seem to be composed of the triangular, plumelike outer parts of the bigger particles.

Figure 10a shows HAP in the solution at pH = 7.5, the original pH of the HAP suspension in a 0.05 M NaCl solution. Individual plume-shaped particles with sizes of around 200−300 nm can be seen in the topography image. Dissolution of the particles was observed immediately after acidification of the solution to pH = 4.0. The decrease in the size and disappearance of the particles can be observed in Figure 10b. However, the particles reprecipitated in approximately 50 min when the system in solution reached equilibrium (Figure 10c). The same effect was also observed

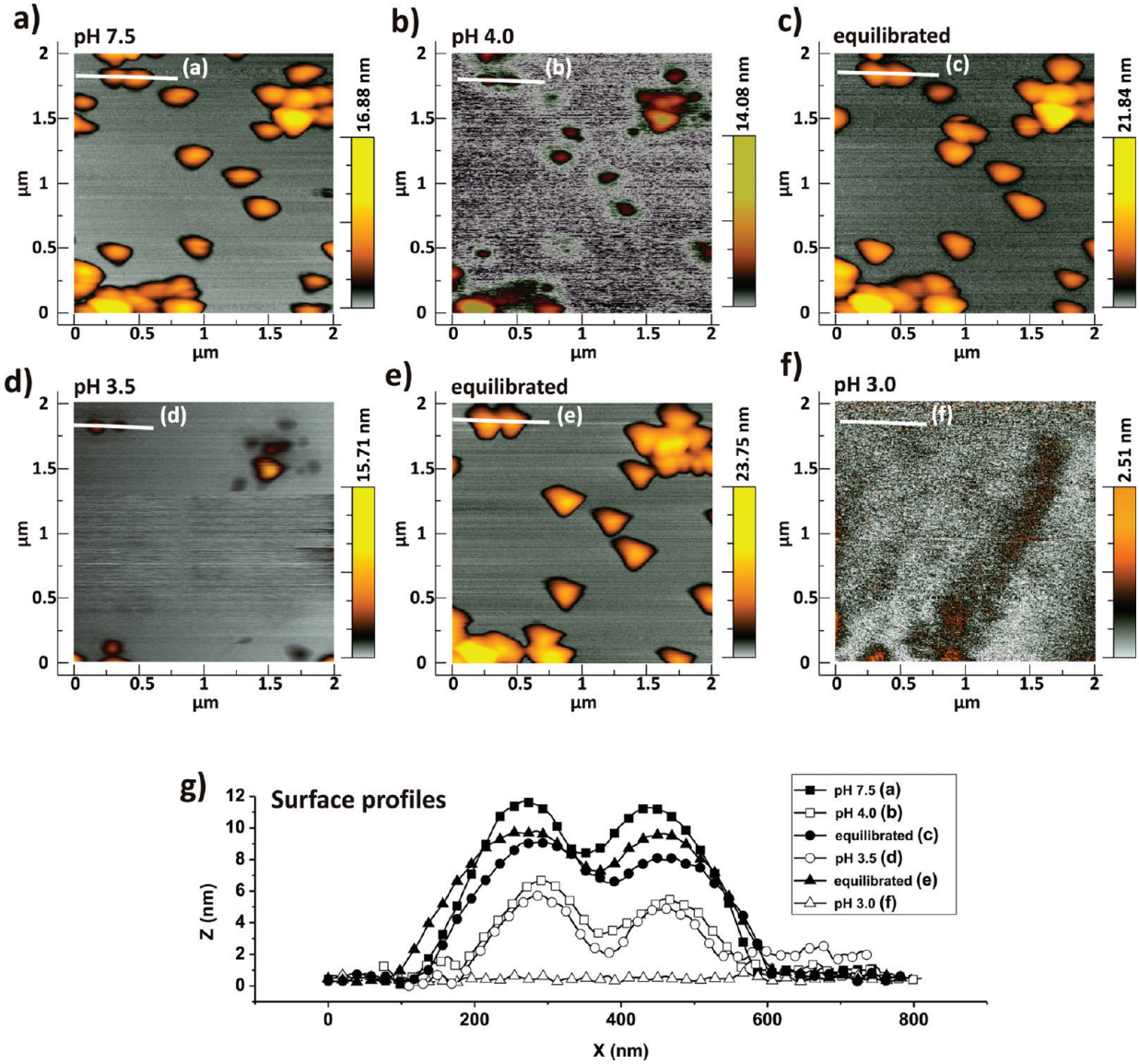

FIGURE 10. AFM topography maps monitoring in situ dissolution of HAP in 0.05 M NaCl at different pHs: (a) pure 0.05 M NaCl, pH = 7.5; (b) pH = 4.0, right after acidification with HCl; (c) pH = 4.0, after equilibrium is reached; (d) pH = 3.5, right after acidification with HCl; (e) pH = 3.5, after equilibrium is reached; (f) pH = 3.0, an equilibrated solution, (g) surface profiles of isolated HAP particles (marked on the AFM images).

at pH = 3.5 (Figure 10d,e). Acidification of the solution leads to partial dissolution of the particles, the structure of which was rebuilt in approximately 50 min. After that, a calculated amount of the HCl solution was injected, making pH = 3.0, and, consequently, the HAP nanoparticles were irreversibly dissolved (Figure 10f). The surface height profiles in Figure 10g clearly show the dimensional change of two selected HAP particles during the measurements.

Evolution of the surface roughness (calculated root mean square, RMS) for the in situ AFM scans (Figure 11) describes the changes in the HAP size during the course of regulated pH variations. While in neutral conditions the RMS value for the selected area was 3.43 nm, the roughness fell to 1.56 nm immediately after acid injection shifted the pH to 4.0. During the next 50 min, the HAP reprecipitated and the initial level of roughness (3.32 nm) was regained. At pH = 3.5, the same dissolution/reprecipitation sequence recurred. However, at stronger acidification (pH = 3.0), when the

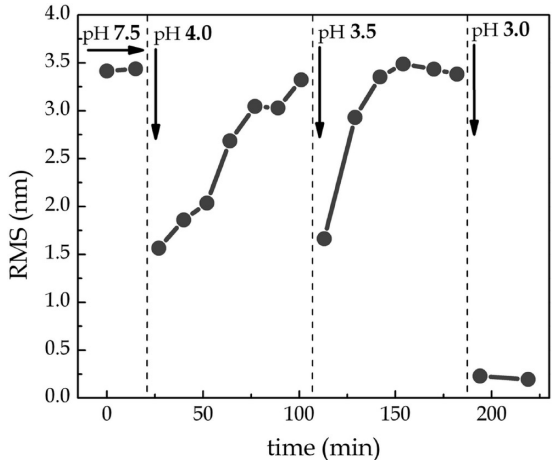

FIGURE 11. Evolution of the RMS roughness calculated from AFM data during the course of in situ solution acidification.

buffering capacity of HAP was exceeded, the RMS roughness decreased to around 0.2 nm; corresponding to the characteristic roughness of smooth mica (001). Thus, reversible dissolution of HAP was observed in the pH range between 4.0 and 3.0.

As reported earlier (19), the nucleation and growth process of the HAP strongly depends on the initial pH. HAP dissolve at acidic pH. The modeling of ionic equilibria relative to Ca^{2+} (see Figure S3 in the SI) predict the initiation of HAP dissolution at pH = 8 that is in good agreement with the release trend of organic inhibitors (Figure 4). The total absence of solid products according to ionic equilibria is predicted for pH lower than 4. Obviously, dissolved phosphate-containing particles are liable to shift the pH back to neutral values, causing particle reprecipitation. Such behavior of the particles can be explained by their buffering effect originating from $PO_4^{3-}-HPO_4^{2-}-H_2PO_4^{-}-H_3PO_4$ and $Cit^{3-}-HCit^{2-}-H_2Cit^{-}-H_3Cit$ equilibria existing in a solution of HAP. The results highlight that HAP are sensitive to pH changes in the acidic range, making them suitable hosts to store corrosion inhibitors to protect aluminum substrates as discussed below.

3.5. pH of the Anodic Dissolution of Aluminum: Modeling and Experimental Measurements. To be used as effective inhibitor reservoirs, HAP have to fulfill several requirements. One of them is the ability to store the inhibitor and release it when the local pH decreases. In spite of the generally accepted idea that anodic dissolution of Al is accompanied by local acidification, the literature provides little confirmation with experimental data. There are very few works (32−34) reporting local pH values of anodic dissolution during the course of corrosion of aluminum alloys. Remarkably, in all three mentioned articles, the measured pH in the anodic sites corresponded to the sensitivity limit of the chosen experimental method. In this work, we measured the local pH of anodic dissolution of Al using pH-selective microelectrodes possessing sensitivity extended into the acidic region.

The anodic dissolution of Al leads to the formation of hydrated Al^{3+} and its hydroxy complexes. A simple calculation shows that the pH values of 0.1, 0.01, 0.001, and 0.0001 M aqueous solutions of Al^{3+} are 2.99, 3.49, 4.01, and 4.56, respectively, due to hydrolysis (eq 1). K^1_{st} was taken from ref 24.

$$Al^{3+}(aq) + H_2O \leftrightarrow [Al(OH)]^{2+}(aq) + H^+(aq)$$
$$pK^1_{hyd} = 4.5 \quad \log K^1_{st} = 9.0 \quad (1)$$

Thus, if the anodic dissolution of Al and reactions of cathodic reduction are separated, the pH at purely anodic sites can fall as low as 3.0−3.5, depending on the intensity of the dissolution and the conditions of ionic diffusion.

It is generally accepted that pitting corrosion of AA2024 begins in the intermetallic inclusions, the so-called S phase, which cover almost 3% of the geometrical surface area of the alloy. These intermetallic zones are composed of

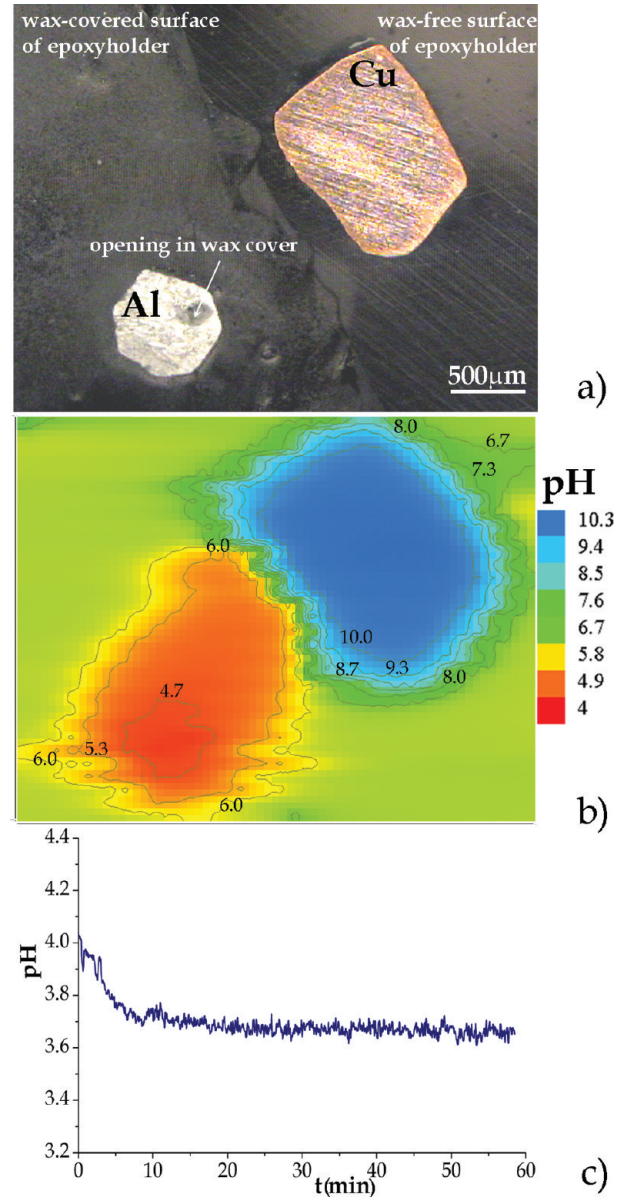

FIGURE 12. (a) Optical micrograph of the zone scanned by SIET. (b) pH distribution over coupled Cu and Al. (c) Evolution of the pH in the confined microdefect made in a beeswax layer covering the Al anode.

Al_2MgCu and, because of the presence of Cu, possess a cathodic potential relative to the alloy matrix, which plays the role of anode in the electrochemical process (21, 35, 36). To model separated anodic and cathodic processes, two electrically coupled strips of pure Cu and Al were embedded in a nonconductive epoxy holder. The localized pH changes induced by the cathodic reduction and anodic dissolution were measured using SIET. The optical micrograph of the area scanned during the SIET measurements and respective pH distribution is presented in Figure 12a,b.

Local alkalinization of the solution over the Cu cathode up to pH = 10.3 and local acidification over Al down to pH = 4.4 were observed after 1 h of immersion in a 0.05 M NaCl solution. Several reproducible scans over the same area were taken throughout 10 h of immersion. All obtained maps can be characterized by pH values of around 4.4−4.2 over the

anodic zone, which are, however, higher than those expected, taking into account intensive dissolution of Al.

To augment the anodic dissolution and impede the diffusion of generated Al^{3+} and H^{+} species, the area of the anode was made even smaller. The polished surface of the Al strip was coated with a thin layer of beeswax and a defect of approximately 250 × 150 μm was made in the beeswax layer to expose a small part of the Al surface. The localized pH was then measured in one single point, inside this confined microdefect. The time-dependent curve of measured pH is presented in Figure 12c. A decrease of the pH down to 3.65 was monitored during the course of Al dissolution.

The results of in situ AFM, release measurements, and local pH monitoring suggest that the HAP are pH-sensitive in the pH range 4−3 corresponding to the local pH of the anodic dissolution of Al. Thus, HAP fulfill the requirement of pH sensitivity and can be used as reservoirs for the storage and controlled release of the corrosion inhibitor. This mechanism is, therefore, responsible for the improved corrosion protection observed in the EIS spectra. Assuming that corrosion occurs in localized defects formed in the oxide layer, underneath the coating, the local pH at the anodes decreases to values that induce partial dissolution of the particles, which, in turn, release part of the inhibitor. The inhibitor forms a protective layer, and the active site is healed. Because the local corrosion activity is hindered, the pH increases again, stopping the particle dissolution and inhibitor release. This can be considered an active anticorrosion system for the protection of aluminum alloys.

CONCLUSIONS

The citrate-modified, calcium-deficient HAP were synthesized to act as submicrometer reservoirs for the corrosion inhibitor.

The results of particle characterization confirm that HAP meet the requirements for inhibitor reservoirs. These include the following: chemical stability and compatibility with the hybrid sol−gel matrix, sufficient loading capacity, ability to sense the corrosion onset (local acidification), and subsequent release of the inhibitor on demand.

HAP provide an anticorrosion effect owing to a two-component protective mechanism: release of the inhibitor and pH buffering resulting from microparticle dissolution. The sensitivity of the HAP to pH is predetermined by their solubility at acidic pH. Local acidification down to pH = 3.65 occurs as a consequence of the anodic dissolution of Al, as shown with localized pH measurements.

The corrosion inhibitors are released during dissolution of the microparticles. The inhibiting effect of both blank and inhibitor-loaded HAP was successfully confirmed on bare and sol−gel-coated 2024 alloys. In both cases, the inhibitor-loaded particles delayed or suppressed the corrosion activity. The blank microparticles demonstrated a certain inhibiting effect that could be ascribed to their pH buffering properties. Thus, ecobenign and easy to produce citrate-modified HAP are proven to be effective anticorrosive agents.

Acknowledgment. We acknowledge financial support from Projects REDE/1509/RME/2005, PTDC/CTM/65632/2006, and PTDC/CTM/108446/2008 (FCT, Portugal) and European FP7 "MUST" NMP3-LA-2008-214261. S.K. thanks FCT for his postdoctoral grant. C. Santos from the University of Aveiro (Aveiro, Portugal) is acknowledged for preparation of the HAP. Prof. G. Grundmeier and Dr. W. Wijting from the University of Paderborn (Paderborn, Germany) are acknowledged for providing the samples with defects made by FIB. Dr. A. S. L. Castela from Instituto Politécnico de Setúbal (Setúbal, Portugal) is acknowledged for his help with HPLC analysis.

Supporting Information Available: Experimental details of HPLC measurements, preparation of pH-selective microelectrodes, experimental, results and discussion of FTIR and XRD characterization of HAP, and modeling of ionic equilibria in a HAP solution. This material is available free of charge via the Internet at http://pubs.acs.org.

REFERENCES AND NOTES

(1) Wang, D.; Bierwagen, G. P. *Prog. Org. Coat.* **2009**, *64*, 327–338.
(2) Metroke, T. L.; Parkhill, R. L.; Knobbe, E. T. *Prog. Org. Coat.* **2001**, *41*, 233–238.
(3) Guglielmi, M. *J. Sol−Gel Sci. Technol.* **1997**, *8*, 443–449.
(4) Zheludkevich, M. L.; Ferreira, M. G. S.; Miranda Salvado, I. M. *J. Mater. Chem.* **2005**, *48*, 5099–5111.
(5) Khramov, A. N.; Voevodin, N. N.; Balbyshev, V. N.; Donley, M. S. *Thin Solid Films* **2004**, *447*, 549–557.
(6) Shchukin, D. G.; Zheludkevich, M. L.; Yasakau, K. A.; Lamaka, S. V.; Ferreira, M. G. S.; Mohwald, H. *Adv. Mater.* **2006**, *18*, 1672–1678.
(7) Yasakau, K. A.; Zheludkevich, M. L.; Lamaka, S. V.; Ferreira, M. G. S. *Proceedings of the 17th International Corrosion Congress*, Las Vegas, NV, Oct 6−10, 2008, p 2720; NACE: Houston, TX, 2008.
(8) Khramov, A. N.; Voevodin, N. N.; Balbyshev, V. N.; Mantz, R. A. *Thin Solid Films* **2005**, *483*, 191–196.
(9) Shchukin, D. G.; Grigoriev, D. O.; Mohwald, H. *Soft Matter* **2010**, *6*, 720–725.
(10) Shchukin, D. G.; Mohwald, H. *Adv. Funct. Mater.* **2007**, *17*, 1451–1458.
(11) Lamaka, S. V.; Zheludkevich, M. L.; Yasakau, K. A.; Serra, R.; Poznyak, S. K.; Ferreira, M. G. S. *Prog. Org. Coat.* **2007**, *58*, 127–135.
(12) Lamaka, S. V.; Zheludkevich, M. L.; Yasakau, K. A.; Montemor, M. F.; Cecílio, P.; Ferreira, M. G. S. *Electrochem. Commun.* **2006**, *8*, 421–428.
(13) Shchukin, D. G.; Lamaka, S. V.; Yasakau, K. A.; Zheludkevich, M. L.; Möhwald, H.; Ferreira, M. G. S. *J. Phys. Chem. C* **2008**, *112*, 958–964.
(14) Poznyak, S. K.; Tedim, J.; Rodrigues, L. M.; Salak, A. N.; Zheludkevich, M. L.; Dick, L. F. P.; Ferreira, M. G. S. *ACS Appl. Mater. Interfaces* **2009**, *1*, 2353–2362.
(15) Decher, G.; Hong, J. D.; Schmitt, J. *Thin Solid Films* **1992**, *210/211*, 831–835.
(16) Lamaka, S. V.; Shchukin, D. G.; Andreeva, D. V.; Zheludkevich, M. L.; Mohwald, H.; Ferreira, M. G. S. *Adv. Funct. Mater.* **2008**, *18*, 3137–3147.
(17) Hiromoto, S.; Yamamoto, A. *Electrochim. Acta* **2009**, *54*, 7085–7093.
(18) Bastidas, D. M.; La Iglesia, V. M.; Criado, M.; Fajardo, S.; La Iglesia, A.; Bastidas, J. M. *Constr. Build. Mater.* **2010**, *24*, 2646–2649.
(19) Martins, M. A.; Santos, C.; Almeida, M. M.; Costa, M. E. V. *J. Colloid Interface Sci.* **2008**, *318*, 210–216.
(20) Santos, C.; Martins, M.; Almeida, M. M.; Costa, M. E. V. *Microsc. Microanal.* **2009**, *15*, 85–86.
(21) Yasakau, K. A.; Zheludkevich, M. L.; Lamaka, S. V.; Ferreira, M. G. S. *J. Phys. Chem. B* **2006**, *110*, 5515–5528.
(22) Lamaka, S. V.; Zheludkevich, M. L.; Yasakau, K. A.; Montemor, M. F.; Ferreira, M. G. S. *Electrochim. Acta* **2007**, *52*, 7231–7247.

(23) Horcas, I.; Fernandez, R.; Gomez-Rodriguez, J. M.; Colchero, J.; Gomez-Herrero, J.; Baro, A. M. *Rev. Sci. Instrum.* **2007**, *78*, 013705.
(24) Lur'e, Y. Y. *Handbook of Analytical Chemistry*, 6th ed.; Himiya, 1989.
(25) In *Stability constants of metal-ion complexes, part B: organic ligands*; Perrin, D., Ed.; Pergamon Press: Oxford, U.K., 1979.
(26) Sarkar, M. *Analyst* **1991**, *116*, 537–541.
(27) Wilson, R. M.; Elliot, J. C.; Dowker, S. E. P. *J. Solid State Chem.* **2003**, *174*, 132–140.
(28) Zheludkevich, M. L.; Serra, R.; Montemor, M. F.; Yasakau, K. A.; Miranda Salvado, I. M.; Ferreira, M. G. S. *Electrochim. Acta* **2005**, *51*, 208–217.
(29) Galio, A. F.; Lamaka, S. V.; Zheludkevich, M. L.; Dick, L. F.; Müller, I. L.; Ferreira, M. G. S. *Surf. Coat. Technol.* **2010**, *204*, 1479–1486.
(30) Yasakau, K.; Zheludkevich, M.; Karavai, O. V.; Ferreira, M. G. S. *Prog. Org. Coat.* **2008**, *63*, 352–361.
(31) Voevodin, N. N.; Grebasch, N. T.; Soto, W. S.; Arnold, F. E.; Donley, M. S. *Surf. Coat. Technol.* **2001**, *140*, 24–28.
(32) Ding, H.; Hawthorn, G. A.; Hihara, L. H. *J. Electrochem. Soc.* **2009**, *156*, C352–C359.
(33) Isaacs, H. S.; Adzic, G.; Jeffcoate, C. S. *Corrosion* **2000**, *56*, 971–978.
(34) Lamaka, S. V.; Taryba, M. G.; Zheludkevich, M. L.; Ferreira, M. G. S. *Electroanalysis* **2009**, *21*, 2447–2453.
(35) Liu, Z.; Chong, P. H.; Butt, A. N.; Skeldon, P.; Thompson, G. E. *Appl. Surf. Sci.* **2005**, *247*, 294–299.
(36) Buchheit, R. G.; Grant, R. P.; Hlava, P. F.; McKenzie, B.; Zender, G. L. *J. Electrochem. Soc.* **1997**, *144*, 2621–2628.

AM1005942